RESEARCH ARTICLE

ADVANCED FUNCTIONAL MATERIALS
www.afm-journal.de

# The Out-of-Plane C—S Bonds Boosting Reversible Redox in Copper Sulfide Cathodes for Ultradurable Magnesium Battery

*Qin Su, Weixiao Wang, Jiajun Chen, Juan Ji, Wenwen Wang, Wen Ren,* Lei Zhang,* Jun Xie,* and Qinyou An**

**As a typical conversion-type cathode material, CuS has shown great potential in the field of rechargeable magnesium batteries (RMBs) due to its excellent energy density, stable voltage platforms, and low cost. However, the poor phase conversion reversibility in CuS cathodes has resulted in low Coulombic efficiency and short cycling life, impeding its further development. Herein, an abundance of C–S heterointerfaces is meticulously crafted by the CuS nanoparticles anchored on rGO nanosheets (CuS@G). The out-of-plane C—S bonds effectively reduce the activation energy of sulfur atoms within Cu-S tetrahedrons, facilitating the formation of S—S bonds in the $Cu_2S$ crystal structure and driving the reversible phase conversion between $Cu_2S$ and CuS during the charge/discharge process. Furthermore, a more reversible phase conversion could diminish copper ion dissolution induced by volume expansion. Consequently, the CuS@G cathode exhibits one of the most remarkable rate performances to date (160.5 mAh $g^{-1}$ at 1 A $g^{-1}$), retaining 64.7% of its capacity after 1000 cycles. Additionally, a durable CuS@G||Mg pouch cell is successfully assembled, delivering a high capacity of 9.5 mAh. These fundamental insights provide valuable guidance for the design of high-performance conversion cathode materials for next-generation RMBs.**

## 1. Introduction

Rechargeable magnesium batteries (RMBs) have emerged as one of the most promising alternatives to Li-ion batteries, thanks to the abundant magnesium resources, enhanced safety, and high volumetric capacity (3833 mAh $cm^{-3}$).[1–3] Significant progress has been made in the development of Mg electrolytes, yet the quest for efficient $Mg^{2+}$ storage cathodes remains an ongoing challenge.[4–6] Presently, two primary categories of inorganic cathode materials are capable of storing $Mg^{2+}$: intercalation-type and conversion-type.[7–9] Intercalation cathodes, such as $V_2O_5$,[10] $MoO_3$,[11] $Mo_6S_8$,[12] $VS_4$,[13] and $WSe_2$,[14] have garnered considerable research interest due to their high operating voltage and minimal voltage hysteresis.[15] However, these materials offer relatively limited specific capacities due to the constraints of fixed-layer spacing.[16] Conversely, conversion cathode materials, which leverage the multivalence states of elements and are not restricted by a rigid lattice structure, exhibit much higher specific capacities.[17,18]

In recent years, the conversion cathode has therefore attracted increasing attention. Among them, CuS, a prototypical conversion-type material, has drawn widespread interest for its theoretical specific capacity of ≈560 mAh $g^{-1}$ and low cost.[19,20] However, its practical application is hindered by the poor reversibility of the conversion reactions.[21,22] Various strategies have been explored to address these challenges. Xu et al. demonstrated that reducing CuS particle size to ≈100 nm can facilitate $Mg^{2+}$ diffusion, achieving reversible conversion from Cu to $Cu_2S$.[23] Similarly, Mai et al. found that combining CuS with MXene can enhance electron transport, thereby improving the reaction kinetics of Cu to $Cu_2S$.[24] Subsequently, Cao et al. proposed that strong Se-C interactions could effectively anchor selenium, suppress its dissolution, and facilitate the redox activity of $Cu^+$.[25]However, despite these advances, the reverse conversion from $Cu_2S$ to CuS remains difficult to achieve.[26]

When comparing the crystal structures of $Cu_2S$ and CuS, it can be inferred that the formation of S—S bonds is a pivotal step in phase conversion.[27] Upon activation, adjacent sulfur atoms in

---

Q. Su, W. Wang, J. Chen, J. Ji, W. Wang, W. Ren, L. Zhang, Q. An
State Key Laboratory of Advanced Technology for Materials Synthesis and Processing
Wuhan University of Technology
Wuhan 430070, P. R. China
E-mail: renwen@whut.edu.cn; zhanglei1990@whut.edu.cn; anqinyou86@whut.edu.cn
J. Xie
State Key Laboratory of Silicate Materials for Architectures
Wuhan University of Technology
Wuhan 430070, P. R. China
E-mail: xiejun2006@whut.edu.cn
Q. An
Hainan Institute
Wuhan University of Technology
Sanya 572000, P. R. China
Q. An
Hubei Longzhong Laboratory
Wuhan University of Technology (Xiangyang Demonstration Zone)
Xiangyang 441000, P. R. China

The ORCID identification number(s) for the author(s) of this article can be found under https://doi.org/10.1002/adfm.202419594

**DOI: 10.1002/adfm.202419594**

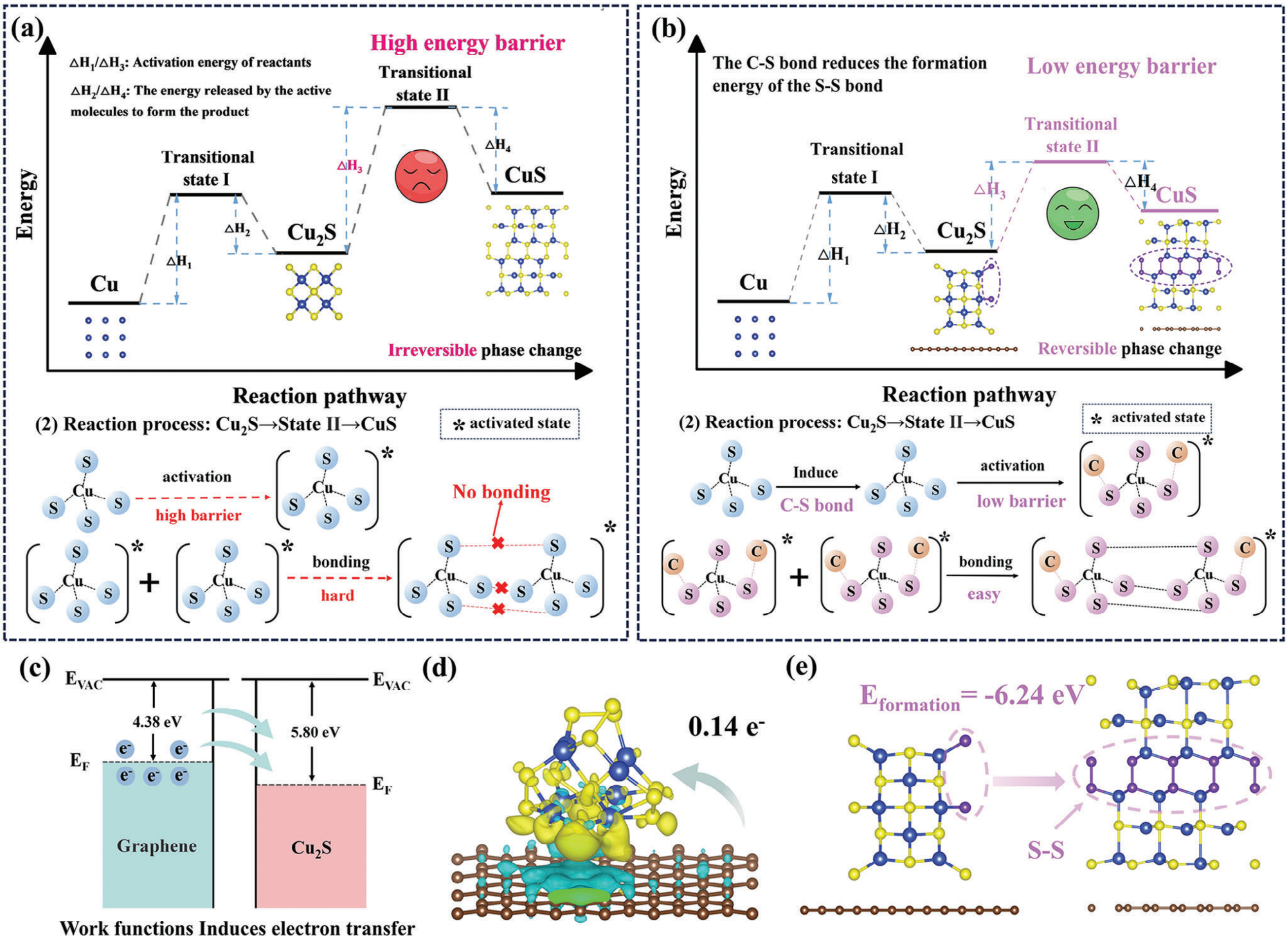

**Figure 1.** Schematic illustration effect of C—S bonds on the phase conversion barrier of the CuS cathode: a) phase conversion process of pure CuS cathode; b) phase conversion process of CuS@G cathode. c) Graphene and $Cu_2S$ work function calculations. d) Charge transfer calculations between $Cu_2S$ and graphene. e) Calculation of the formation energy of S—S bonds.

$Cu_2S$ spontaneously combine to form more stable S—S bonds.[28] However, $Cu_2S$ possesses a relatively stable Cu—S tetrahedral structure, which results in a high activation energy for the sulfur atoms and a substantial S—S bond formation energy (**Figure 1a**). Thus, reducing the formation energy of S—S bonds and lowering the energy barrier for $Cu_2S$ to CuS conversion are the primary challenges for CuS cathode materials.

In this context, we propose the introduction of C—S bonds to diminish the energy barrier for the $Cu_2S$ to CuS conversion (Figure 1b). The presence of C—S bonds effectively reduces the activation energy of sulfur atoms within the Cu-S tetrahedrons, lowers the formation energy of S—S bonds, and facilitates the conversion from $Cu_2S$ to CuS during the charging process. DFT calculations were employed to validate this approach. The work function calculations indicate that electrons flow from graphene to sulfur atoms in $Cu_2S$ (Figure 1c; Figure S1, Supporting Information). Further charge differential analysis reveals a charge transfer of 0.14 $e^-$ (Figure 1d; Figure S2, Supporting Information), rendering the sulfur in $Cu_2S$ unstable and promoting the formation of S—S bonds. As shown in Figure 1e, under the influence of C—S bonds, the formation energy of S—S bonds is calculated to be −6.24 eV (Figure 1e; Figures S3 and S4, Supporting Information).

Moreover, enhanced phase conversion alleviates stress, reduces the dissolution of Cu ions caused by particle disintegration, and effectively prevents Cu ion deposition from damaging the solid-electrolyte interphase (SEI) of the magnesium anode. These remarkable attributes have led to one of the most impressive rate performances to date (160.5 mAh $g^{-1}$ at 1 A $g^{-1}$), with a capacity retention of 64.7% after 1000 cycles. More significantly, a sustainable CuS@G||Mg pouch cell was successfully assembled, boasting a peak capacity of 9.5 mAh. These findings underscore the critical role of C—S bonds in reversible phase conversion and the mitigation of Cu dissolution in CuS, unlocking new avenues for the design of high-performance cathode materials for RMBs.

## 2. Results and Discussion

### 2.1. Morphology and Structure Characterisation

CuS@G was synthesized using a template method as depicted in Figure S5 (Supporting Information). The introduction of the

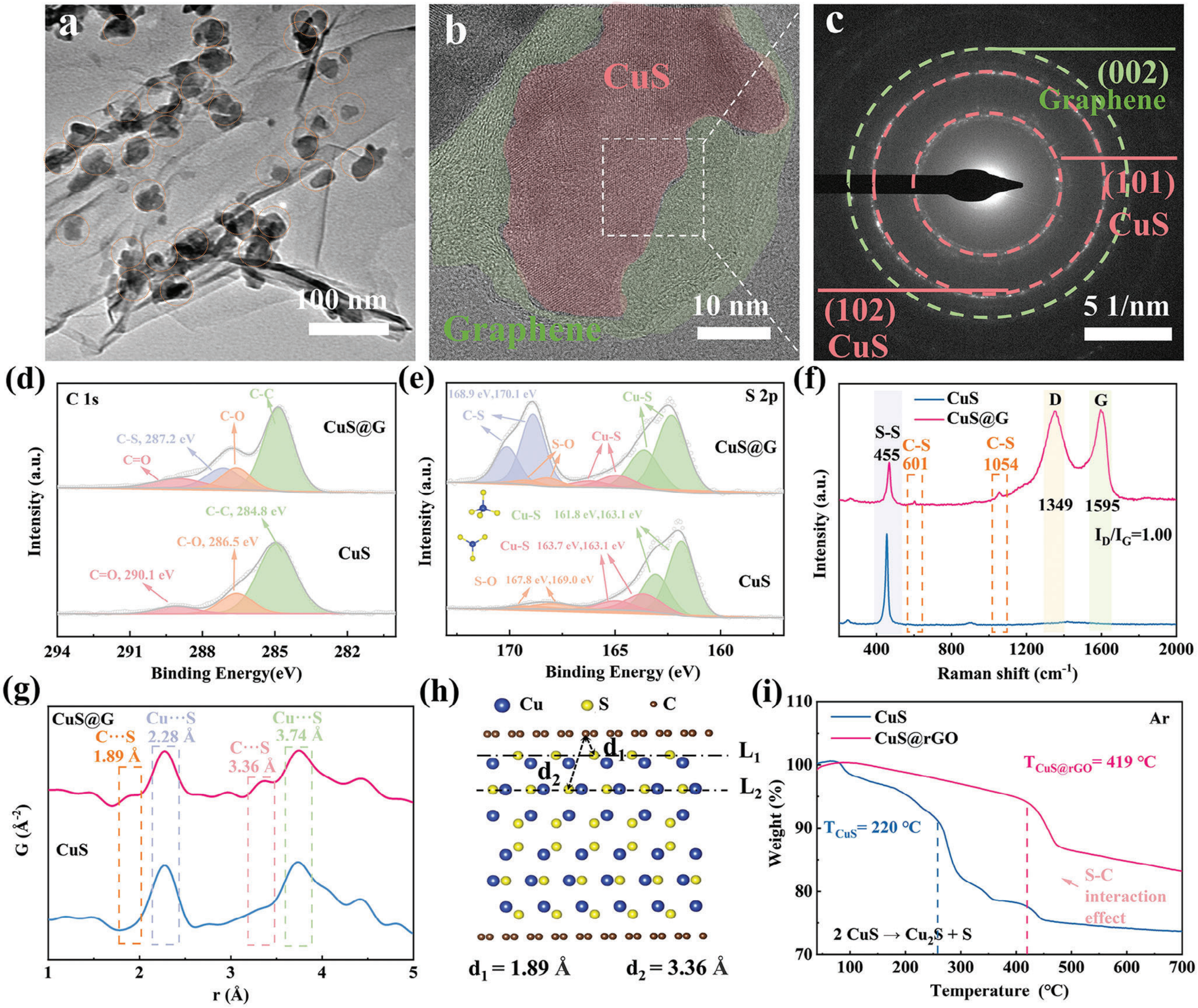

**Figure 2.** Morphological and structural characterizations of CuS@G. a) TEM images. b) HRTEM images. c) SAED pattern. High-resolution XPS spectra: d) C 1s and e) S 2p. f) Raman spectra. g) Plot of the pair distribution function. h) Schematic diagram of the C—S bond distribution. i) Thermogravimetric curves (Ar).

templating agent, tris-aminomethane (THAM), moderates the nucleation rate, allowing for the in situ growth of small CuS particles (diameter <50 nm) on graphene. Subsequently, hydrazine hydrate ($N_2H_4$), acting as a reducing agent, was employed to remove any residual template.

After preparation, the morphologies of CuS@G and pristine CuS were characterized using scanning electron microscopy (SEM) and transmission electron microscopy (TEM). SEM images revealed that CuS nanoparticles were uniformly distributed across the graphene matrix (Figures S6 and S7, Supporting Information). Furthermore, the particle size remained relatively unchanged after compositing with graphene, with diameters consistently below 50 nm. TEM images of CuS@G illustrated that some CuS particles were dispersed on the surface of the graphene sheets, while others were encapsulated (**Figure** 2a), corroborating the SEM findings. High-resolution TEM (HRTEM) analysis identified two types of lattice fringes in CuS@G. The well-defined lattice spacing of 3.23 Å corresponds to the (101) plane of hexagonal CuS, while the blurred green regions indicate amorphous graphene (Figure 2b). Moreover, the gradual transition of the lattice fringes into an amorphous phase without a distinct domain boundary suggests a degree of bonding between CuS and graphene (Figure S8, Supporting Information). Selected area electron diffraction (SAED) patterns further confirmed this interaction, displaying diffraction spots corresponding to the (110) and (102) planes of polycrystalline CuS, alongside the (002) plane of graphene (Figure 2c). The composite structure of CuS@G was also verified by energy-dispersive X-ray spectroscopy (EDX), which showed even distribution of copper and sulfur across a carbon substrate, with atomic ratio close to 1:1 (Figure S9, Supporting Information).

The interaction between CuS particles and graphene was further explored using X-ray diffraction (XRD), X-ray photoelectron spectroscopy (XPS), Raman spectroscopy, and Pair Distribution Function (PDF) analysis. XRD patterns (Figure S10a, Supporting Information) confirmed that all samples shared the same crystal structure, belonging to covellite (CuS, JCPDS No. 06–0464). XPS C 1s spectra (Figure 2d) exhibited peaks at 284.8, 286.5, and 288.7 eV in pure CuS, corresponding to C—C, C—O, and C═O bonds, respectively. In CuS@G, a new peak at 287.2 eV was observed, indicative of a strong C–S interaction. The XPS spectra in Figure 2e further confirmed the presence of C—S bonds in CuS@G. The intensive S 2p peaks of CuS@G were deconvoluted into four pairs of peaks. The peaks at 161.8 and 163.1 eV represent Cu—S bonds, where copper is coordinated with four sulfur atoms. The adjacent peaks at 163.7 and 163.1 eV also correspond to Cu—S bonds, where copper coordinates with three sulfur atoms. The peaks at 167.8 and 169.0 eV correspond to S—O bonds, likely arising from the oxidation of the CuS surface. All three pairs of peaks appear consistently in both the CuS and CuS@G spectra. Notably, strong new peaks at 168.9 and 170.1 eV were attributed to the C—S bonds formed between graphene and CuS, indicating an abundance of C—S bonds in the graphene/CuS heterojunction. This interaction led to a 0.3 eV shift in the XPS spectra of Cu LMM (Figure S10b,c, Supporting Information).

The Raman spectrum of pure CuS displays a distinct peak at 455 $cm^{-1}$, which corresponds to the S—S bond within the crystal structure. In contrast, the Raman spectra of CuS@G (Figure 2f) reveal characteristic peaks of graphene at 1349 $cm^{-1}$ (D band) and 1595 $cm^{-1}$ (G band). Additionally, the emergence of new peaks at 601 and 1054 $cm^{-1}$ can be attributed to the interaction of C—S bonds (Figure S11, Supporting Information). PDF analysis was also employed to probe the short-range local electronic structures, offering further insights into the bonding interactions between CuS and graphene.[29] As shown in Figure 2g, two new peaks at 1.89 and 3.36 Å appear in the CuS@G spectrum. Based on the schematic diagram of CuS@G (Figure 2h), the new peak at 1.89 Å corresponds to the bond between the outermost sulfur atoms ($L_1$) and graphene, while the peak at 3.36 Å corresponds to the bond between the sub-outer sulfur atoms ($L_2$) and graphene. Upon refining the PDF curve, it was found that the introduction of C—S bonds led to an increase in the CuS unit cell parameters (Figure S12 and Table S1, Supporting Information), which may also explain the reduction in S—S bond formation energy.

Thermogravimetric analysis (TGA) was conducted in an Ar atmosphere within a temperature range of 25–700 °C. Pure CuS thermally decomposes at 220 °C in Ar, yielding S and $Cu_2S$ as decomposition products.[30] However, after compositing with graphene, the decomposition temperature of CuS increased significantly to 419 °C, nearly doubling its original value. The strong C–S interactions likely contribute to stabilizing the crystal structure of CuS, thereby greatly enhancing its thermal stability (Figure 2i). TGA performed in air allowed for the calculation of the graphene content in CuS@G, which was ≈20% (Figure S13, Supporting Information).[31] Furthermore, an investigation into the impact of the graphene-to-copper sulfide ratio on performance demonstrated that optimal results are attained at a graphene content of 20% (Figure S14, Supporting Information).

## 2.2. Effect of the C—S Bond on Electrochemical Performance

To further explore the impact of the C—S bond on the electrochemical properties, the samples' electrochemical behaviors were evaluated. As shown in **Figure 3a**, the incorporation of graphene markedly alters the cyclic voltammetry (CV) curves. In the first three cycles, the reduction peak intensity of pure CuS gradually diminishes, while the peak intensity of CuS@G remains largely unchanged. Additionally, after the initial two cycles of activation, the CV curves of pure CuS display two reduction peaks at 1.75 and 1.90 V. In contrast, CuS@G exhibits three distinct reduction peaks at 1.54, 1.80, and 1.90 V during the third cycle. This suggests a different charging reaction mechanism compared to pure CuS. The shared peak at 1.90 V is likely associated with electrolyte decomposition.[32]

Theoretically, during charging, CuS cathodes exhibit two plateaus, corresponding to the conversion of Cu to $Cu_2S$ and $Cu_2S$ to CuS.[33] However, in the first three cycles, pure CuS consistently displays only one charging plateau at 1.75 V (Figure 3b). This phenomenon, widely reported in previous studies, is attributed to the irreversible formation of S—S bonds during charging, which causes the active material to transition from its initial CuS state to $Cu_2S$.[34] In contrast, the strongly interacting C—S bonds in CuS@G promote the formation of S—S bonds, allowing for two distinct charge plateaus at 1.54 and 1.80. The 1.54 V plateau corresponds to the Cu to $Cu_2S$ conversion, while the 1.80 V plateau represents the $Cu_2S$ to CuS transition. This indicates that the C—S bond facilitates the formation of CuS, aligning with the results of the CV tests. Furthermore, CuS@G demonstrates a reduced activation energy of 27.6 kJ $mol^{-1}$, affirming that C—S bonds play a pivotal role in diminishing the activation energy of sulfur atoms within $Cu_2S$ (Figure S15, Supporting Information). In the first cycle, the discharge capacities of CuS@G and pure CuS are quite similar. However, by the second cycle, CuS@G achieves a significantly higher discharge capacity of 254.5 mAh $g^{-1}$, compared to 208.1 mAh $g^{-1}$ for pure CuS. Moreover, both CuS and CuS@G exhibit high $Mg^{2+}$ diffusion coefficients and conductivity, further confirming their favorable electrochemical performance (Figures S16 and S17, Supporting Information).

The cyclic and rate properties of the samples were further examined, revealing significant differences in cycling stability between CuS@G and pure CuS. The pure CuS cathode experiences rapid capacity decay during cycling, while the CuS@G cathode maintains a stable capacity of 212 mAh $g^{-1}$ and 83.2% capacity retention after 100 cycles at 100 mA $g^{-1}$ (Figure 3c,d). As shown in Figure 3e, the CuS@G cathode exhibits remarkable improvements in rate performance. At a current density of 50 mA $g^{-1}$, it delivers capacities exceeding 280 mAh $g^{-1}$ (Figure S18, Supporting Information). Even when the current is progressively increased to 1 A $g^{-1}$, the CuS@G cathode retains a capacity of 160.5 mAh $g^{-1}$, corresponding to 57.3% of its initial capacity.

For transition-metal sulfides, structural pulverization is a well-known issue that leads to significant capacity decay.[35] Based on previous reports, the capacity ramp-up phenomenon, typical of transition metal sulfides, is often associated with particle pulverization. The slope height during the activation process may

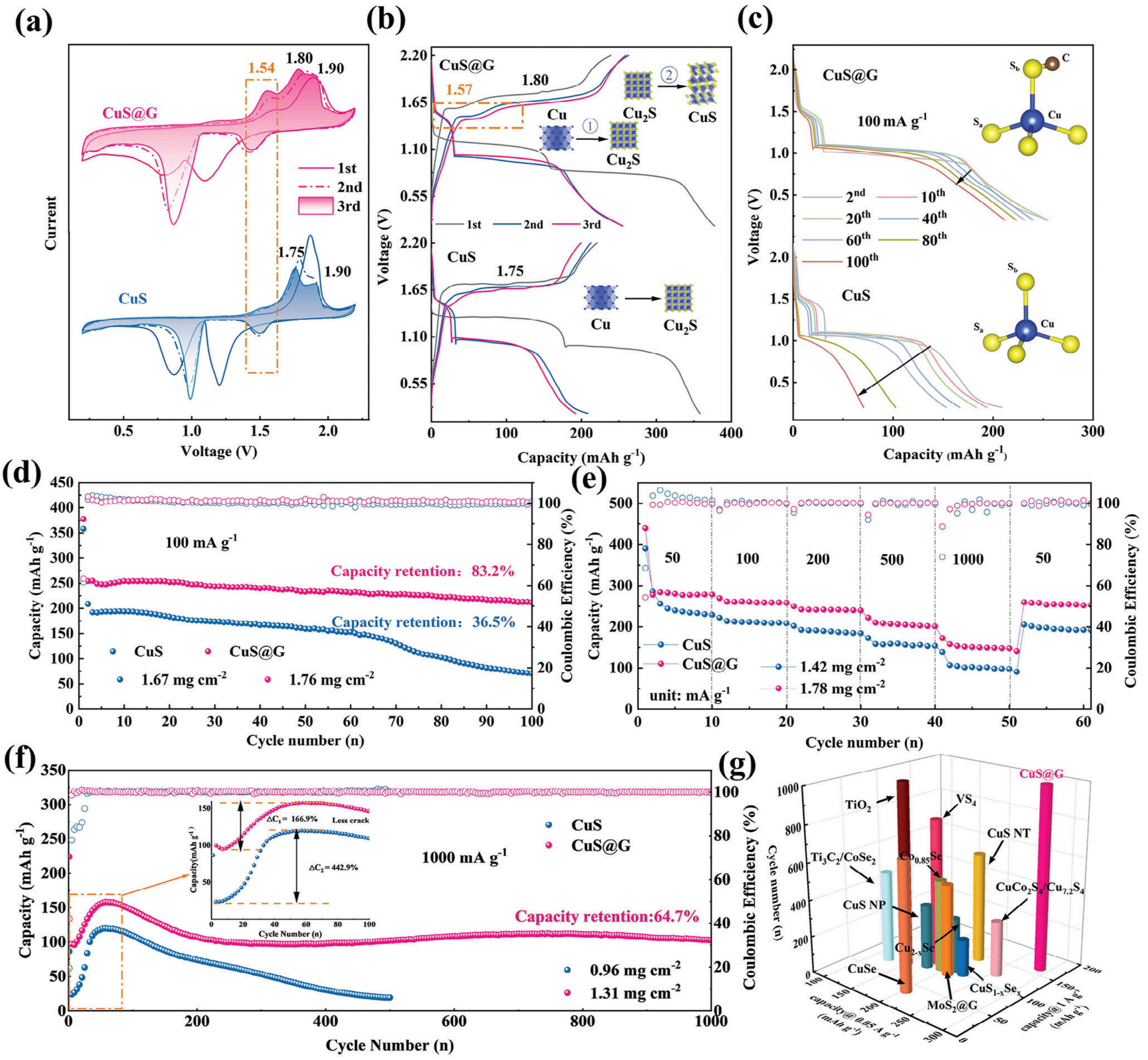

**Figure 3.** Electrochemical behaviors. a) CV plots (0.1 mV s$^{-1}$). Galvanostatic charge and discharge profiles of b) 50 mA g$^{-1}$ and c) 100 mA g$^{-1}$. d) Cycling performance and Coulombic efficiencies at current densities of 100 mA g$^{-1}$. e) Rate capabilities at current densities of 50 to 1000 mA g$^{-1}$. f) Cycling performance and Coulombic efficiencies at current densities of 1000 mA g$^{-1}$. g) Comparison of electrochemical performance with previously reported cathode materials.

indicate the material's resistance to crushing. Figure 3f demonstrates that CuS@G exhibits a low ramp-up of 166.9% (58 mAh g$^{-1}$) at 1000 mA g$^{-1}$, compared to 442.9% (99.5 mAh g$^{-1}$) for pure CuS. The rapid capacity decay in the pure CuS cathode is a result of particle pulverization, leading to its eventual failure in subsequent cycles. However, the CuS@G cathode retains 64.7% (101.7 mAh g$^{-1}$) of its capacity after 1000 cycles at 1000 mA g$^{-1}$. The enhanced resistance to pulverization can be attributed to the C—S bond, which promotes reversible phase conversion, thereby alleviating stress accumulation and particle fracturing. Remarkably, even compared to other reported RMB cathode materials, the CuS@G cathode exhibits the highest capacity at 1 A g$^{-1}$ (Figure 3g; Table S2, Supporting Information).

### 2.3. Facilitation of Reversible Phase Transitions

To confirm the role of the C—S bond in promoting phase conversion, ex situ Raman and XRD spectroscopy were conducted. Ex situ Raman spectroscopy was used to observe the variation of the S—S bond during the first cycle. As shown in **Figure 4a**, when discharged to 0.2 V, the S—S bond in pure CuS vanishes. During the subsequent charging process, it proves difficult for the S—S

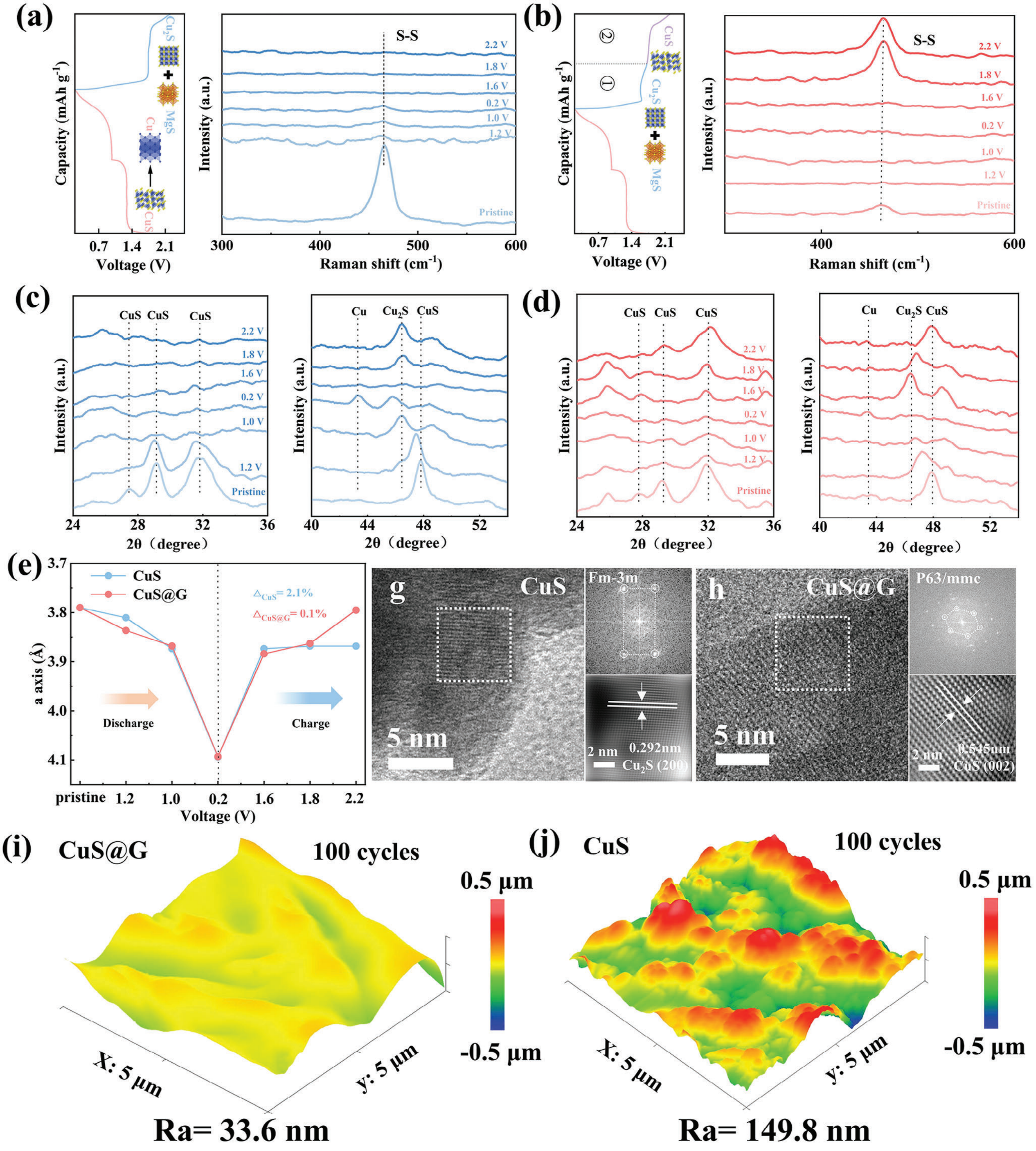

**Figure 4.** Effect of C—S bonds on reversible phase transitions. Ex situ Raman patterns of a) CuS and b) CuS@G electrodes at different electrochemical states. Ex situ XRD patterns of c) CuS and d) CuS@G electrodes at different electrochemical states. e) a-axis change of pure CuS and CuS@G during the charge and discharge process. HAADF-STEM images of g) CuS and h) CuS@G electrodes at the final charging state. Surface roughness comparison of i) CuS@G and j) pure CuS before and after 100 cycles, area 5 × 5 µm.

bond in pure CuS to reform. However, in the case of CuS@G, a strong S—S bond is formed during charging (Figure 4b), indicating that the C—S bond effectively promotes the formation of the S—S bond, which is consistent with the theoretical calculations.

Ex situ XRD analysis was performed to further investigate the phase conversion process during the first cycle (Figure 4c,d). Before cycling, both pure CuS and CuS@G cathodes show the typical hexagonal CuS phase. After discharging to 0.2 V, the diffraction peaks corresponding to the CuS phase weaken, and new Cu and MgS phases emerge. Both samples undergo a similar phase conversion process during discharge. However, after charging to 2.2 V, pure CuS transitions to $Cu_2S$ (cubic phase), and further conversion to CuS (hexagonal phase) is difficult (Figure S19, Supporting Information).

In contrast, CuS@G, influenced by the C—S bond, undergoes a distinct phase transition process during charging. When charged to 1.6 V, Cu gradually converts to $Cu_2S$, and by 1.8 V, $Cu_2S$ transitions back to CuS. Eventually, all $Cu_2S$ is fully converted to CuS (Figures S20 and S21 and Table S3, Supporting Information). The unit cell parameters, particularly the a-axis, were analyzed throughout the cycling process. Pure CuS undergoes a transformation into $Cu_2S$ after cycling, with its crystal structure changing from cubic to tetragonal, leading to a 2.1% change along the a-axis (Figure 4e). In contrast, with the assistance of the C—S bond, CuS@G undergoes a reversible phase conversion with minimal change in the a-axis, indicating a lower accumulation of stress during cycling.

TEM was employed to further examine the morphology and phase composition in the fully charged state. For the pure CuS electrode, severe particle crushing and agglomeration were observed after cycling, likely resulting from stress accumulation within the particles due to an irreversible phase transition (Figure S22a, Supporting Information). In contrast, the CuS@G electrode maintained its morphology, which can be attributed to the C—S bond's role in facilitating reversible phase conversion (Figure S22b, Supporting Information).

Moreover, HRTEM images revealed differences in phase composition between the two electrodes at the end of charging. As shown in Figure 4g, the final product of the pure CuS electrode is a cubic phase (Fm-3m), with lattice spacings of 0.292 nm corresponding to the $Cu_2S$ (200) plane. Conversely, the end-state product of the CuS@G electrode is a hexagonal phase (P63/mmc), with lattice spacings of 0.545 nm corresponding to the CuS (002) plane (Figure 4h). This further confirms that the C—S bond plays a crucial role in promoting the reversible phase conversion of CuS.

The 3D morphology of the cycled pure CuS and CuS@G cathodes was further examined. The CuS@G cathode exhibited minimal surface roughness (Ra = 33.6 nm, Figure 4i; Figure S23a, Supporting Information) after 100 cycles, indicating a uniform and stable interface. This smoothness contributes to maintaining structural integrity and delivering superior electrochemical performance. In contrast, the pure CuS cathode showed significantly higher surface roughness (Ra = 149.8 nm, Figure 4j; Figure S23b, Supporting Information). Several large bulges (highlighted in red) were observed on the surface of the pure CuS electrode, likely due to severe swelling, uncontrolled solid-electrolyte interphase (SEI) growth, and particle pulverization during repeated cycling.

The volume expansion behavior of the CuS and CuS@G electrodes after 100 cycles was also studied using SEM. Cross-sectional SEM images revealed that the electrode thickness of pure CuS dramatically increased from 25.2 to 66.9 µm after 100 cycles, resulting in an alarming expansion rate of 265.5% (Figure S24a,b, Supporting Information). Furthermore, top-view SEM images showed extensive surface cracks and significant pulverization of active particles on the surface of the pure CuS electrode (Figure S24c,d, Supporting Information). Such particle crushing and crack formation are highly undesirable, as they hinder charge transport across the electrode and may even isolate active particles, thereby degrading electrochemical performance.[36]

In contrast, the CuS@G electrode exhibits only a minor variation in thickness, increasing from 20 to 21.3 µm, with a modest expansion rate of 106.3% (Figure S24e,f, Supporting Information). After 100 cycles, no cracks or particle agglomeration are observed on the surface of the CuS@G electrode, indicating enhanced structural stability and resistance to degradation compared to the pure CuS electrode (Figure S24e,f, Supporting Information). This stability is likely due to the promoting effect of the C—S bond, which promotes reversible phase transitions and reduces stress build-up inside the particles throughout repeated cycling.

### 2.4. Inhibits the Dissolution of the Cu Element

Through the analysis of the magnesium anode after 100 cycles, the shuttling of Cu and S elements during cycling was further investigated. As shown in **Figure 5**a, a significant amount of metallic copper ($Cu^0$) was detected on the surface of the Mg anode corresponding to the pure CuS electrode, and its content increased with the depth of etching. This indicates that during cycling, Cu ions from the pure CuS electrode dissolve into the electrolyte and deposit on the magnesium anode as Cu metal. Although the content of $Cu^0$ on the Mg anode surface from CuS@G also increases with etching time, it remains consistently at a much lower level (Figure 5b). Inductively coupled plasma mass spectrometry (ICP-MS) analysis further reveals that the $Cu^0$ shuttle from the pure CuS electrode is 0.056%, nearly four times higher than that of the CuS@G electrode, which shows a $Cu^0$ shuttle of only 0.014% (Table S4, Supporting Information). This reduced shuttle may result from the fact that CuS@G particles experience less fragmentation during cycling, leading to fewer Cu ions migrating to the Mg anode.

Observation of the circulating diaphragm also confirms that the CuS@G cathode exhibits less copper shuttling (Figure S25, Supporting Information). A polysulfide (MgS×) signal at ≈162 eV is detected on the surface of the Mg anode from the pure CuS electrode. In contrast, the Mg anode corresponding to CuS@G shows not only the $MgS_x$ signal but also an additional S—O peak. This suggests the formation of two distinct solid-electrolyte interphases (SEIs) on the surface of the Mg anodes (Figure S26, Supporting Information). Additionally, the two Mg anodes show a slight difference in MgS× content, which may be due to the low quantity of MgS×, and the semi-quantitative nature of XPS analysis (Figure S27, Supporting Information).

The impact of Cu shuttling on the SEI of the Mg anode was further investigated through time-of-flight secondary ion mass

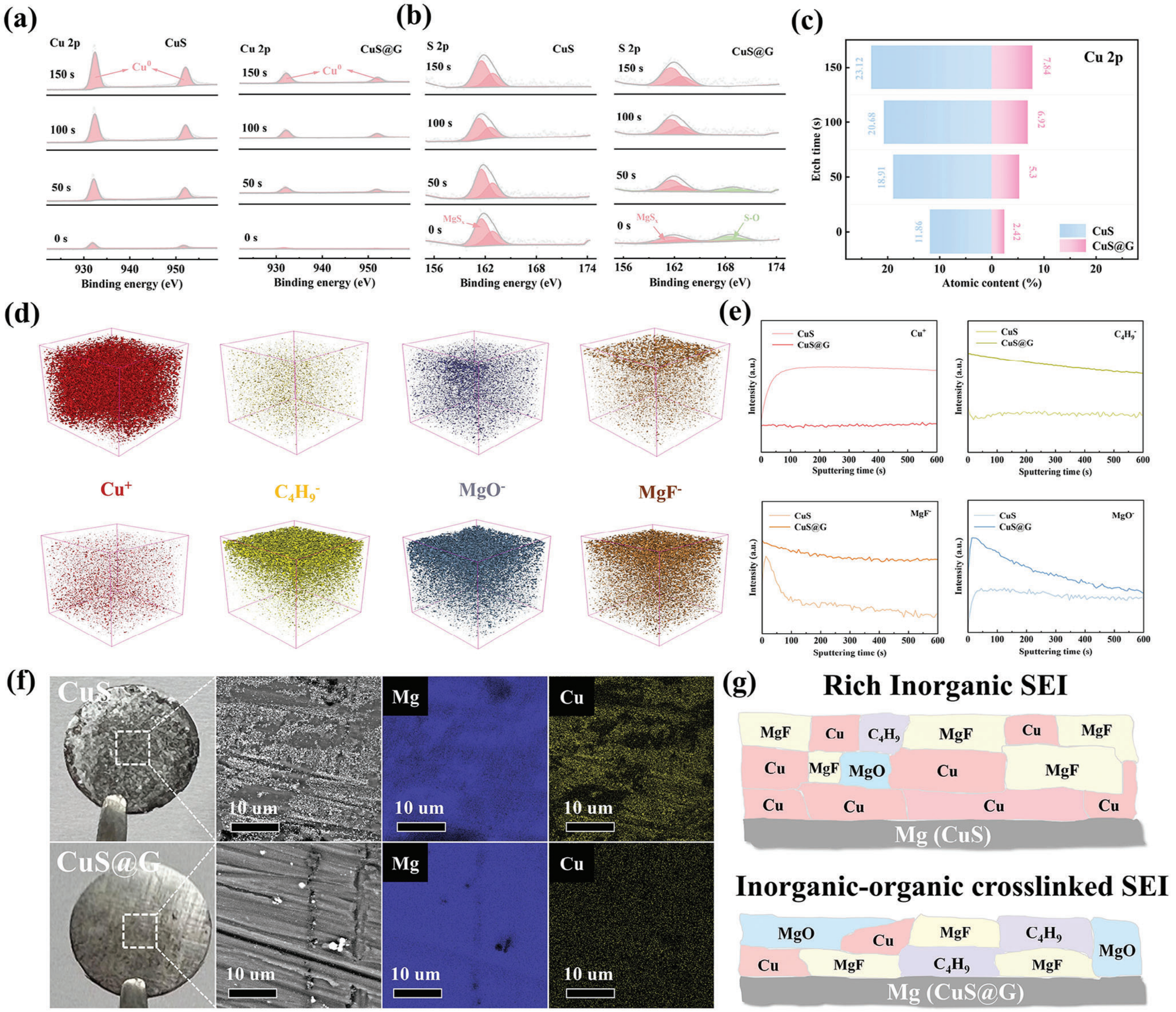

**Figure 5.** Characterization of the magnesium anode. a) The corresponding XPS spectra of Cu 2p and S 2p on the Mg anode after 100 cycles. b) Cu element content deposited on Mg anodes probed by XPS at different etch times. c) and d) 3D reconstruction of $Cu^+$, $C_4H_9^-$, $MgO^-$, and $MgF^-$ fragments on the at surface of the Mg anodes after 100 cycles. e) Photograph and SEM image of the magnesium anode after 100 cycles, along with the corresponding mapping of the elemental distribution of Cu (yellow) and Mg (blue). f) Schematic diagram of the effect of copper ion dissolution on the SEI of Mg anode.

spectrometry (TOF-SIMS), and 3D surface reconstruction was performed to examine the components of the Mg anode surface after 100 cycles. As shown in Figure 5c,d, in the pure CuS system, excessive copper accumulates on the surface of the magnesium anode, resulting in a thin SEI enriched with inorganic components. The thinning of the SEI occurs because the copper occupies most of the surface area of the magnesium anode, hindering the growth of the SEI.[37] The SEI becomes enriched with inorganic components due to redox reactions between $Cu^+$ ions from the electrolyte and the anionic group $OC(CF_3)_3$, which promote the release of more $F^-$ ions, thus reducing the $MgF_2$ content within the SEI. This rigid, inorganic-rich SEI is insufficient to protect the Mg anode from $Cl^-$ corrosion (Figure S28, Supporting Information).

In contrast, under the influence of C—S bonds in the CuS@G electrode, fewer Cu elements dissolve and deposit on the Mg anode, resulting in an SEI that consists of both organic ($C_4H_9^-$) and inorganic ($MgO^-$, $MgF^-$) components. This organic–inorganic hybrid SEI effectively protects the Mg anode, likely contributing to the superior electrochemical performance and reduced capacity fade of CuS@G compared to pure CuS.[33] The inability of the pure CuS electrode to form such a protective SEI may explain its rapid capacity decay.

Moreover, optical and SEM images of the Mg anode after cycling reveal differences in the size and quantity of CuS particles deposited on the two Mg anodes (Figure 5e). The Mg anode paired with the CuS@G electrode shows fewer and smaller Cu particles, consistent with the findings from XPS and TOF-SIMS

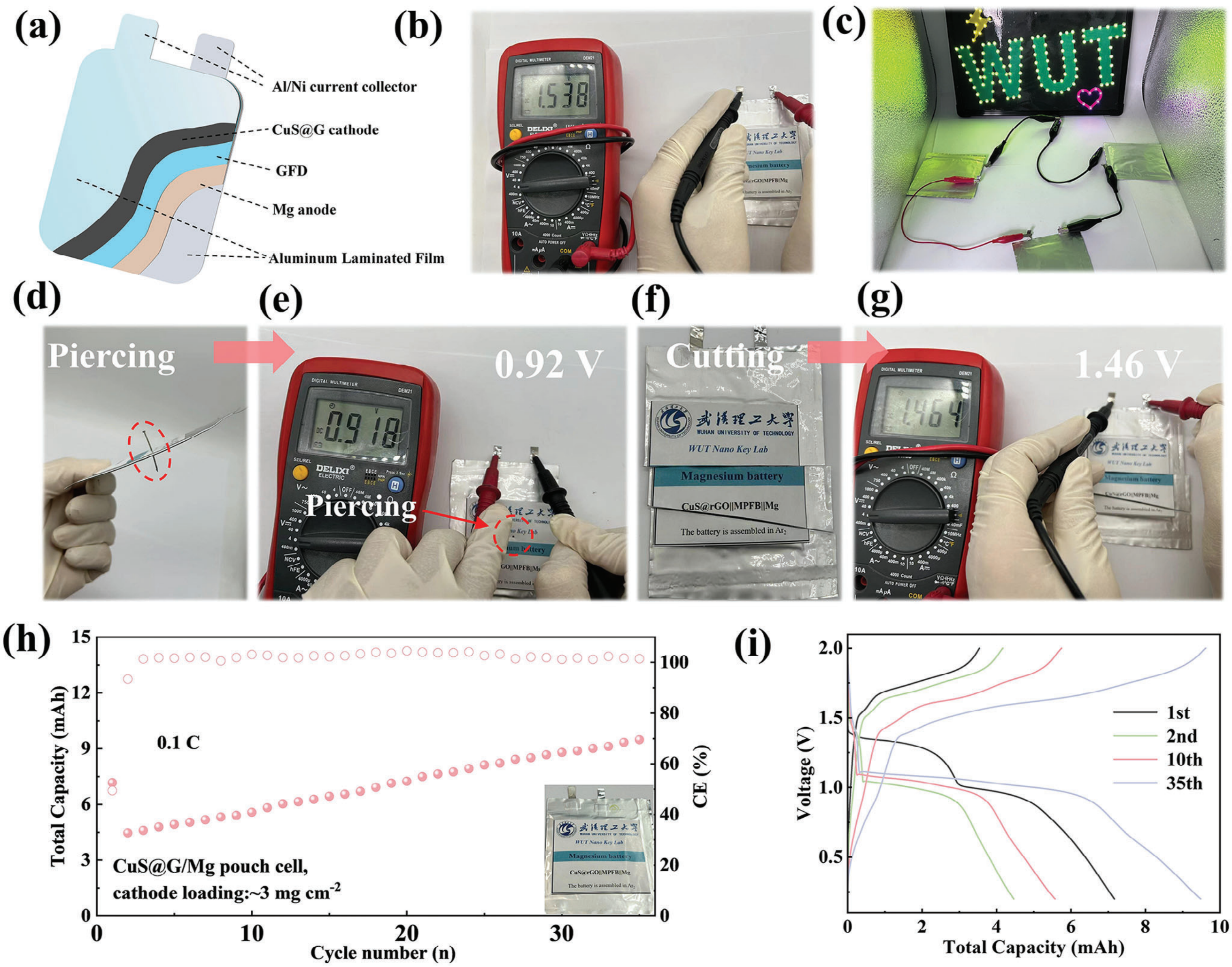

**Figure 6.** Pouch cell performances. a) Schematic diagram of the soft package structure, b) Open circuit potential of the CuS@G||Mg pouch cell. c) Lighted LEDs by the CuS@G||Mg pouch cells in MPFB electrolytes. d–g) Extreme conditions tested. h) Cycling performance of the CuS@G||Mg pouch cell at 0.1 C. i) Charge-discharge profiles of pouch cell after the first, second, 10th, and 35th cycles.

analyses. Overall, it is evident that the C─S bond facilitates a reversible phase transition that minimizes Cu dissolution and protects the SEI on the Mg anode from degradation, as illustrated in Figure 5f and Figure S29 (Supporting Information).

### 2.5. Pouch Cell Performance

Thus far, the exceptional physicochemical properties of the CuS@G electrode have been thoroughly evaluated. Owing to the unique C─S bond in CuS@G, CuS@G||Mg coin cells demonstrated excellent electrochemical performance. These promising results motivated us to develop practical and sustainable CuS@G||Mg pouch cells. The components of the CuS@G||Mg pouch cells are illustrated in **Figure 6a**. Specifically, a CuS@G cathode with dimensions of 5 × 5 cm and a high mass loading of ≈3 mg cm$^{-2}$ was prepared, while magnesium foil (≈120 µm thick, Figure S30, Supporting Information) was selected as the anode for the pouch cell fabrication.

CuS@G||Mg pouch cells using MPFB electrolyte were successfully assembled and used to power a light-emitting diode (LED) board (Figures 6b,c). To assess safety, the pouch cells were subjected to both a nail penetration test and a cutting test. Remarkably, even after being pierced and undergoing multiple cuts, the pouch cell continued to function without short circuits or combustion, demonstrating the exceptional safety of these cells (Figure 6d–g).

Following assembly, the CuS@G||Mg pouch cell underwent electrochemical charging and discharging processes. After activation, the pouch cell delivered a total capacity of 9.5 mAh, with a gravimetric energy density of 138.6 Wh kg$^{-1}$ (Figure 6h,i). These highly encouraging results confirm that the CuS@G electrode maintains excellent performance even when assembled into CuS@G||Mg pouch cells. The demonstrated feasibility of using CuS@G for high-energy electrode preparation, along with the promising cell performance, paves the way for the accelerated development of sustainable magnesium-metal batteries, contributing to a more sustainable future.

## 3. Conclusion

In this study, we discovered that the strongly interacting C—S bonds facilitate the transfer of electrons from graphene to the sulfur atoms in $Cu_2S$. These additional electrons disrupt the stable Cu-S tetrahedral structure, making it easier for S—S bonds to form between sulfur atoms. The lower formation energy of the S—S bonds ultimately promotes the conversion from $Cu_2S$ to CuS. Additionally, this more reversible phase transition leads to reduced stress accumulation, which in turn minimizes the shuttling of active material (Cu). The reduced Cu shuttling to the anode helps form a composite SEI on the Mg anode, consisting of both inorganic ($C_4H_9^-$) and organic ($MgO^-$, $MgF^-$) components. Owing to these advantages, the CuS@G cathode exhibits one of the best rate performances reported to date, achieving 160.5 mAh $g^{-1}$ at 1 A $g^{-1}$, with a capacity retention of 64.7% after 1000 cycles. Moreover, the sustainable CuS@G||Mg pouch cell was successfully assembled, demonstrating a high capacity of 9.5 mAh. In principle, the beneficial effect of the C—S bond could be extended to other conversion-type cathodes (e.g., $CoS_2$, $NiS_2$, $FeS_2$), enhancing the reversibility of their conversion reactions and reducing active material shuttling.

## Supporting Information

Supporting Information is available from the Wiley Online Library or from the author.

## Acknowledgements

Q.S., and W.W. contributed equally to this work. This work was supported by the National Key Research and Development Program of China (No. 2023YFB3809501), the National Natural Science Foundation of China (52172231), the Natural Science Foundation of Hubei Province (2022CFA087, 2024AFB040, and 2022CFD089). Supported by Key Research and Development Program of Hubei (2022BAA027).

## Conflict of Interest

The authors declare no conflict of interest.

## Data Availability Statement

The data that support the findings of this study are available from the corresponding author upon reasonable request.

## Keywords

Mg battery, C—S bonds, sulfide redox, reversible phase conversion, copper sulfide

Received: October 16, 2024
Revised: November 3, 2024
Published online: November 21, 2024

---

[1] Q. Sun, S. Luo, R. Huang, S. Yan, X. Lin, *Coord. Chem. Rev.* **2024**, *515*, 215956.
[2] D. Wang, Z. Zhang, Y. Hao, H. Jia, X. Shen, B. Qu, G. Huang, X. Zhou, J. Wang, C. Xu, F. Pan, *Adv. Funct. Mater.* **2024**, *34*, 202410406.
[3] Z. Fan, R. Li, X. Zhang, W. Zhao, Z. Pan, X. Yang, *Nano-Micro Lett.* **2025**, *17*, 4.
[4] S. Li, J. Zhang, S. Zhang, Q. Liu, H. Cheng, L. Fan, W. Zhang, X. Wang, Q. Wu, Y. Lu, *Nat. Energy* **2024**, *9*, 285.
[5] H. Zhou, W. Sun, X. Su, M. Liu, Z. Zhou, A. Du, S. Dong, Q. Wang, Z. Zhang, G. Li, G. Cui, *Angew. Chem., Int. Ed.* **2024**, *63*, 202415540.
[6] Y. Man, P. Jaumaux, Y. Xu, Y. Fei, X. Mo, G. Wang, X. Zhou, *Sci. Bull.* **2023**, *68*, 1819.
[7] Z. Zhang, S. Dong, Z. Cui, A. Du, G. Li, G. Cui, *Small Methods* **2018**, *2*, 1800020.
[8] M. Zhang, S. Feng, Y. Wu, Y. Li, *Acta Phys. Chim. Sin.* **2022**, *0*, 2205050.
[9] M. Wu, Z. Zhou, *Interdiscip. Mater.* **2023**, *2*, 231.
[10] W. Wang, W. Wang, F. Xiong, J. Meng, J. Wu, W. Yang, J. Long, J. Chen, J. Chen, Q. An, *Angew. Chem., Int. Ed.* **2024**, *63*, 202414119.
[11] W. Wang, F. Xiong, S. Zhu, M. Yan, X. Liao, K. Yu, L. Cui, J. Chen, J. Wang, R. Lan, J. Xie, Q. An, L. Mai, *Natl. Sci. Rev.* **2024**, *11*, nwae238.
[12] D. Wang, X. Du, G. Chen, F. Song, J. Du, J. Zhao, Y. Ma, J. Wang, A. Du, Z. Cui, X. Zhou, G. Cui, *Angew. Chem., Int. Ed.* **2023**, *62*, 202217709.
[13] X. Zhang, Q. Tang, Y. Liu, Y. Zhu, J. Zhang, J. Wang, R. Shi, *Chem. Eng. J.* **2024**, *497*, 154966.
[14] T. Huang, X. Xue, Y. Zhang, M. Cui, Y. Zhang, L. Chen, B. Xiao, J. Qi, Y. Sui, *Small* **2024**, *20*, 2404898.
[15] C. Qiu, H. Huang, M. Yang, L. Xue, X. Zhu, Y. Zhao, M. Ni, T. Chen, H. Xia, *Energy Storage Mater.* **2024**, *72*, 103736.
[16] J. Heo, S.-K. Jung, I. Hwang, S.-P. Cho, D. Eum, H. Park, J.-H. Song, S. Yu, K. Oh, G. Kwon, T. Hwang, K.-H. Ko, K. Kang, *Nat. Energy* **2022**, *8*, 30.
[17] W. Li, D. Wang, *Adv. Mater.* **2023**, *36*, 2304983.
[18] Z. Li, G. Zhou, S. Li, H. Liu, L. Wang, H. Li, *Joule* **2023**, *7*, 2609.
[19] Y. Shen, Y. Wang, Y. Miao, M. Yang, X. Zhao, X. Shen, *Adv. Mater.* **2020**, *32*, 1905524.
[20] D. Tao, T. Li, Y. Tang, H. Gui, Y. Cao, F. Xu, *Adv. Funct. Mater.* **2024**, *34*, 2411223.
[21] Y. Fei, H. Wang, Y. Xu, L. Song, Y. Man, Y. Du, J. Bao, X. Zhou, *Chem. Eng. J.* **2024**, *480*, 148255.
[22] X. Chen, X. Xie, P. Ruan, S. Liang, W.-Y. Wong, G. Fang, *ACS Energy Lett.* **2024**, *9*, 2037.
[23] M. Wu, Y. Zhang, T. Li, Z. Chen, S. Cao, F. Xu, *Nanoscale* **2018**, *10*, 12526.
[24] Z. Cheng, Y. Xu, X. Zhang, Q. Peng, K. Wang, X. Zhang, X. Sun, Q. An, L. Mai, Y. Ma, *J. Mater. Chem. A* **2023**, *11*, 12176.
[25] C. Du, Y. Zhu, Y. Zhang, H. Peng, J. Tian, T. Xia, L. Yang, X. Liu, X. Ma, C. Cao, *Energy Storage Mater.* **2023**, *61*, 102863.
[26] G. Whang, W. G. Zeier, *ACS Energy Lett.* **2023**, *8*, 5264.
[27] X. Gao, J. Tian, S. Cheng, Z. Zuo, R. Wen, F. He, Y. Li, *Angew. Chem., Int. Ed.* **2023**, *62*, 202304491.
[28] L. Tan, A. Li, Y. Yang, J. Zhang, X. Niu, N. Li, L. Liu, L. Guo, Y. Zhu, *Angew. Chem., Int. Ed.* **2022**, *61*, 202206012.
[29] M. Kløve, S. Sommer, B. B. Iversen, B. Hammer, W. Dononelli, *Adv. Mater.* **2023**, *35*, 2208220.
[30] Y. Fei, Y. Man, J. Sun, Y. Du, B. Chen, J. Bao, X. Zhou, *Small* **2023**, *19*, 2301954.
[31] S. Foley, H. Geaney, G. Bree, K. Stokes, S. Connolly, M. J. Zaworotko, K. M. Ryan, *Adv. Funct. Mater.* **2018**, *28*, 1800587.

[32] J. Xiao, X. Zhang, H. Fan, Q. Lin, L. Pan, H. Liu, Y. Su, X. Li, Y. Su, S. Ren, Y. Lin, Y. Zhang, *Adv. Energy Mater.* **2022**, *12*, 2202602.

[33] Y. Xia, C. Chen, L. Ran, H. Zhang, S. Cui, P. Xiao, F. Xu, D. Zhang, T. Li, *Chem. Eng. J.* **2024**, *488*, 151133.

[34] C. Du, S. He, L. Yang, X. Liu, R. Jiang, X. Ma, Y. Zhu, M. Zou, C. Cao, *Energy Storage Mater.* **2024**, *70*, 103539.

[35] Z. Zhang, K. Dong, K. A. Mazzio, A. Hilger, H. Markötter, F. Wilde, T. Heinemann, I. Manke, P. Adelhelm, *Adv. Energy Mater.* **2023**, *13*, 2203143.

[36] Q. Fang, S. Xu, X. Sha, D. Liu, X. Zhang, W. Li, S. Weng, X. Li, L. Chen, H. Li, B. Wang, Z. Wang, X. Wang, *Energy Environ. Sci.* **2024**, *17*, 6368.

[37] M. Ma, R. Huang, M. Ling, Y. Hu, H. Pan, *Interdiscip. Mater.* **2023**, *2*, 833.